Capacitive Micromachined Ultrasonic Transducers: Next-Generation Arrays for Acoustic Imaging?

Ömer Oralkan, *Student Member, IEEE*, A. Sanlı Ergun, *Associate Member, IEEE*, Jeremy A. Johnson, *Student Member, IEEE*, Mustafa Karaman, *Member, IEEE*, Utkan Demirci, *Student Member, IEEE*, Kambiz Kaviani, *Student Member, IEEE*, Thomas H. Lee, *Member, IEEE*, and Butrus T. Khuri-Yakub, *Fellow, IEEE*

Abstract—**Piezoelectric materials have dominated the ultrasonic transducer technology. Recently, capacitive micromachined ultrasonic transducers (CMUTs) have emerged as an alternative technology offering advantages such as wide bandwidth, ease of fabricating large arrays, and potential for integration with electronics. The aim of this paper is to demonstrate the viability of CMUTs for ultrasound imaging. We present the first pulse-echo phased array B-scan sector images using a 128-element, one-dimensional (1-D) linear CMUT array. We fabricated 64- and 128-element 1-D CMUT arrays with 100% yield and uniform element response across the arrays. These arrays have been operated in immersion with no failure or degradation in performance over the time. For imaging experiments, we built a resolution test phantom roughly mimicking the attenuation properties of soft tissue. We used a PC-based experimental system, including custom-designed electronic circuits to acquire the complete set of 128×128 RF A-scans from all transmit-receive element combinations. We obtained the pulse-echo frequency response by analyzing the echo signals from wire targets. These echo signals presented an 80% fractional bandwidth around 3 MHz, including the effect of attenuation in the propagating medium. We reconstructed the B-scan images with a sector angle of 90 degrees and an image depth of 210 mm through offline processing by using RF beamforming and synthetic phased array approaches. The measured 6-dB lateral and axial resolutions at 135 mm depth were 0.0144 radians and 0.3 mm, respectively. The electronic noise floor of the image was more than 50 dB below the maximum mainlobe magnitude. We also performed preliminary investigations on the effects of crosstalk among array elements on the image quality. In the near field, some artifacts were observable extending out from the array to a depth of 2 cm. A tail also was observed in the point spread function (PSF) in the axial direction, indicating the existence of crosstalk. The relative amplitude of this tail with respect to the mainlobe was less than −20 dB.**

Manuscript received January 21, 2002; accepted July 24, 2002. This work was supported by the United States Office of Naval Research and CBYON, Inc.

Ö. Oralkan and K. Kaviani are with the Edward L. Ginzton Laboratory, Stanford University, Stanford, CA 94305-4088 and the Center for Integrated Systems, Stanford University, Stanford, CA 94305-4070 (e-mail: ooralkan@stanford.edu).

A. S. Ergun, M. Karaman, U. Demirci, and B. T. Khuri-Yakub are with the Edward L. Ginzton Laboratory, Stanford University, Stanford, CA 94305-4088.

J. A. Johnson is with the Department of Neurosurgery, Image Guidance Laboratory, School of Medicine, Stanford University, Stanford, CA 94305-5327.

T. H. Lee is with the Center for Integrated Systems, Stanford University, Stanford, CA 94305-4070.

I. Introduction

Acoustical devices have been used for practical underwater imaging applications since World War I. Use of ultrasound in medicine started in the 1930s. Piezoelectric crystals (e.g., Rochelle salt and quartz) and magnetostrictive materials (e.g., nickel) were the transduction material of choice until the 1940s. The intense materials research during World War II gave birth to the second generation of transduction materials, the piezoelectric ceramics (e.g., barium titanate and lead zirconate titanate). Electronic sector scanning for ultrasonic diagnosis was introduced in the late 1960s. The tensile piezoelectricity in stretched and poled films of polyvinylidene fluoride (PVDF), a polymer, was demonstrated in 1969. Linear arrays with electronic scanning started replacing fixed-focus mechanical sector scanners in the 1970s, providing greatly improved resolution and faster image formation. The details of the history of ultrasound imaging and transducer technologies outlined can be found in several books [1], [2] and papers [3]–[5].

In recent years, advances in microelectronics and digital signal processing technology have enabled processing large amounts of data from transducer arrays with large element counts. The flexibility of digital data processing systems has sparked significant research efforts to develop new algorithms to reconstruct, enhance, and analyze ultrasound images. However, the ability and usefulness of these algorithms depend on the quality (e.g., SNR, bandwidth, and dynamic range) of the original echo signal, making the transducer and associated front-end electronics the most critical components of ultrasound imaging systems.

Throughout the history of ultrasound imaging, piezoelectric crystals, ceramics, polymers, and recently piezocomposite materials [6] have been used to generate and detect ultrasound. Although the idea of capacitive ultrasound transducers is as old as the early piezoelectric transducers, piezoelectric materials have dominated ultrasonic transducer technology. The reason why capacitive transducers have not been popular is that electric field strengths on the order of a million volts per centimeter (10^6 V/cm) are required, so that electrostatic forces as large as a kilo-

gram per square centimeter (kg/cm^2) would be achieved; as the eminent French physicist Paul Langevin stated in 1915 [2]. However, recent advances in microfabrication technology have made it possible to build capacitive ultrasound transducers competing with piezoelectric transducers. Moreover, CMUTs offer advantages of improved bandwidth, ease of fabrication of large arrays with individual electrical connections, and integration with electronics [7].

CMUT technology is not simply a low-cost replacement of piezoelectric transducer technology. Many features inherent in CMUT technology enable revolutionary advances in ultrasound imaging. Currently, real-time volumetric imaging is the focus of extensive research in ultrasound [8]–[10]. The realization of such systems depends on design and fabrication of 2-D transducer arrays. There are difficulties in fabricating these arrays due to limitations in the existing transducer array and interconnect technologies. CMUTs are fabricated using standard silicon integrated circuit (IC) fabrication technology. This technology makes it possible to fabricate large arrays using simple photolithography. Individual electrical connections to transducer elements are provided by through-wafer interconnects. Two-dimensional CMUT arrays with as many as 128×128 elements already have been successfully fabricated and characterized [11]. These 2-D arrays can be integrated with electronics in the form of a 3-D multichip module by flip-chip bonding [12].

Another enabling feature inherent to CMUT technology is wide bandwidth. A wideband transducer does not simply increase the resolution, but it also enables the design of new image modalities and analysis tools. A prominent area of research in medical ultrasound is tissue harmonic imaging, in which energy is transmitted at a fundamental frequency and an image is formed from the energy at the second harmonic [13]. In current harmonic imaging systems, the transmit frequency is set to 2/3 of the center frequency and the receive frequency is set to 4/3 of the center frequency of the transducer, resulting in suboptimal operation both in transmit and receive [14]. CMUTs provide a flat response over a wide frequency range, enabling optimal tissue harmonic imaging.

CMUTs also are promising for high-frequency applications such as intravascular ultrasound imaging (IVUS), in which high-frequency operation using miniature probes is vital. CMUTs operating at frequencies as high as 60 MHz have been fabricated and tested successfully [15]. Experimental front-looking and side-looking IVUS arrays also have been designed and fabricated. Another area of extensive research is ultrasonic tissue characterization, often based on spectral analysis [16] and subband processing [17] of backscattered signals, in which wide bandwidth is crucial.

CMUTs have many promising applications other than medical and underwater imaging as well. Air-coupled, nondestructive evaluation [18], microphones with RF [19] and optical [20] detection schemes, surface and bulk acoustic wave devices [21], and smart microfluidic channels [15] are among these applications.

Since the first demonstration of CMUTs in the early 1990s, extensive research has been conducted on fabrication and modelling of this new transducer technology [22]–[24]. The fabrication process for CMUTs was reported earlier [25], [26]. A transducer equivalent circuit based on Mason's model [27] has been developed [28], and the validity of the model has been confirmed by experimental results [29]. One-dimensional linear CMUT arrays have been characterized, including the acoustical crosstalk in these arrays [30]. Finite element analysis also is an important part of research used to understand the transducer characteristics (especially crosstalk issues) and to optimize the transducer response [31]–[34]. The 2-D receive PSF of a 64-element 1-D linear CMUT array has been measured experimentally and is reported in [35]. The first pulse-echo phased array images using a 16-element, 1-D linear CMUT array were presented in [36].

The aim of this paper is to present the first pulse-echo phased array B-scan sector images using a 128-element, 1-D linear CMUT array to demonstrate the viability of CMUTs for ultrasound imaging, especially for medical and underwater applications. The organization of this paper is as follows. Section II briefly explains the operation and fabrication of CMUTs. The experimental methods used in this study are explained in Section III. Section IV describes the image reconstruction procedure. In Section V, the resulting images are presented and a quantitative analysis is carried out, in which the experimental results are compared with theoretical expectations. Section VI discusses the effects of crosstalk on the reconstructed images. Section VII gives conclusions.

II. CMUT Arrays

A. Principles of Operation

The basic building block of a CMUT is a capacitor cell consisting of a metalized membrane (top electrode) suspended above a heavily doped silicon substrate (bottom electrode) as shown in Fig. 1(a). A single element in the array consists of many small capacitor cells connected in parallel as shown in Fig. 1(b). A top view of four elements of a 1-D CMUT linear array is shown in Fig. 1(c). During CMUT operation, a direct current voltage is applied between the metalized membrane and the substrate. The membrane is attracted toward the bulk by the electrostatic force, and induced stress within the membrane resists the attraction. Driving the membrane with an alternating voltage generates ultrasound. If the biased membrane is subjected to ultrasound, a current output is generated due to the capacitance change under constant bias voltage. The amplitude of this current output is a function of the frequency of the incident wave, the bias voltage, and the capacitance of the device. The efficiency of CMUTs is determined by the electromechanical transformer ratio, which can be expressed as the product of the device capacitance and the electric field strength across

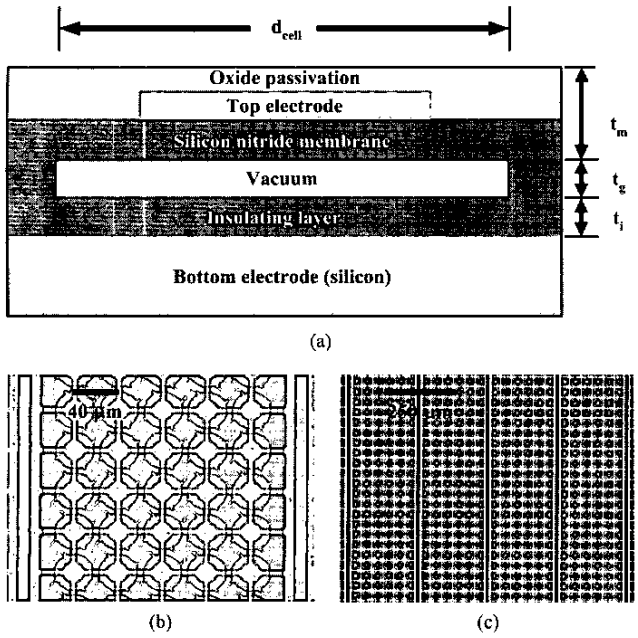

Fig. 1. 1-D CMUT array. (a) Schematic cross section of a CMUT cell. (b) Magnified view of a single 5-cell wide, 1-D array element. (c) A portion of four elements of the 1-D CMUT array.

TABLE I
PHYSICAL PARAMETERS OF THE CMUT ARRAY.

Number of elements in the array (N)	128
Length of an element, μm	6000
Width of an element, μm	200
Element pitch (d), μm	250
Number of cells per element	750
Cell diameter (d_{cell}), μm	36
Membrane thickness (t_m), μm	0.9
Gap thickness (t_g), μm	0.11
Insulating layer thickness (t_i), μm	0.2
Silicon substrate thickness, μm	500

the gap beneath the membrane. Planar fabrication enables building a thin membrane above a submicron sealed cavity, which is crucial to obtain high electric fields for improved transducer performance. The physical dimensions of the 1-D CMUT array used in this work are listed in Table I.

B. Fabrication

The CMUTs are fabricated using standard silicon IC fabrication technology. The details of the CMUT fabrication process can be found in earlier reports [25], [26]. Here, the fabrication process will be summarized briefly to give an outline for the reader. First, the silicon wafer is doped heavily through diffusion and drive-in for formation of the bottom electrode of the capacitor. Then, a layer of silicon nitride is deposited as a protective insulator for the bottom electrode and as an etch stop. An amorphous silicon layer is deposited over the wafer. This layer of amorphous

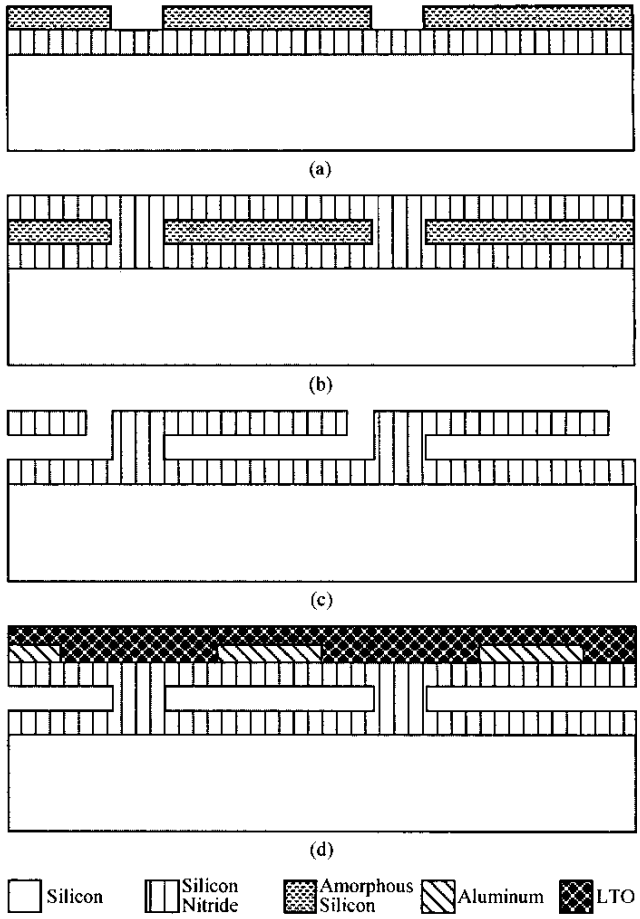

Fig. 2. Basic process steps in CMUT fabrication.

silicon is patterned by photolithography and dry etching, so that the amorphous silicon remains where the vacuum gaps would be formed as shown in Fig. 2(a). A second silicon nitride layer is deposited over the patterned amorphous silicon in order to form the membrane as shown in Fig. 2(b). Small through-holes are defined at the edges of the membrane to allow the etchant to come in contact with amorphous silicon as shown in Fig. 2(c). Potassium hydroxide (KOH) provides the high etch selectivity needed to remove the sacrificial amorphous silicon and release the membrane. Silicon nitride is deposited once again to seal the etch holes. This step is performed at low pressure so that the gap beneath the membrane is evacuated prior to sealing. The top electrode is formed by aluminum metallization. The size and location of the top electrode affect the device performance significantly [33]. A layer of low-temperature-oxide (LTO) is deposited to passivate the device as shown in Fig. 2(d). A total of 6 masks are used in fabrication. The total number of masks for fabrication of 2-D arrays with through-wafer interconnects is 11. The ability to seal the gaps enables immersive operation of CMUTs by preventing the hydrolysis of water in the cavity under high electric fields and loading at the back of

the membrane. Sealing also improves the performance of air transducers by decreasing the loss due to squeeze-film effects [37].

C. Reliability and Yield

Recent improvements in our fabrication process provide better control of the gap height and membrane thickness. These improvements also enable isolation of individual cells in an array element by the separation of etch channels and active areas [38]. As a result, 64- and 128-element 1-D CMUT arrays were fabricated on the same wafer with 100% yield, and no device failure was observed during immersion operation. In this paper, we present the experimental results from the 128-element array. We have performed impedance measurements on the individual array elements in air to demonstrate the yield and uniformity of element response. For impedance measurements, the 128-element 1-D CMUT array was biased at 28 V, a low voltage level to avoid collapsing the membranes. The impedance of each individual element was measured in air using a vector network analyzer (model 8751A, Hewlett-Packard Co., Palo Alto, CA). The device capacitance values and the resonant frequency in air were extracted for each element from the impedance measurements. The results of these measurements are presented in Fig. 3. The mean value of the device capacitance is 27 pF with a standard deviation of 1.75 pF. The mean value of the resonance frequency in air is 12.1 MHz with a standard deviation of 120 kHz. These measurements show that the 128-element 1-D CMUT array has a 100% yield in the number of functional elements, and the uniformity across the array is remarkable. One should note that the resonant frequency in air is given only to demonstrate the uniformity of the array elements. In immersion applications, the mechanical impedance of the medium dominates the impedance of the membrane, resulting in a broadband, nonresonant transducer response.

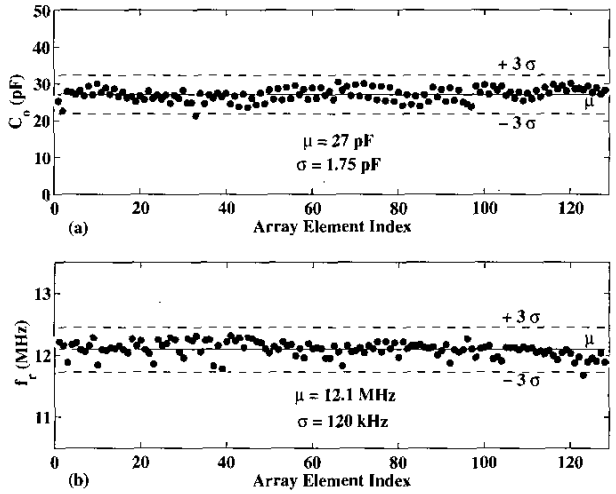

Fig. 3. Measured array statistics. (a) Device capacitance measured across the 128-element array. (b) Resonant frequency in air measured across the 128-element array.

III. Experimental Work

A. Data Acquisition System

The PC-based data acquisition system included custom-designed circuits and a software interface. The experimental setup and the corresponding block diagram are shown in Figs. 4 and 5, respectively. A 128-element, 1-D linear CMUT array was attached and wire bonded onto a printed circuit board (PCB) to provide individual electrical connections to each transducer element. The second PCB along the signal path provided the DC bias to the transducer elements, and alternating current (AC) coupled the transmit and receive signals to and from the array, respectively. A second stage of electronic circuits provided transmit and receive channel selection and amplification of the incoming echo signals. Typically the system is used for collecting A-scans from all transmit-receive channel combinations, in which case only one transmit channel and eight receive channels are selected at a time. For the imaging results presented in this paper, the DC bias voltage on the CMUT array was set to 40 V for maximum sensitivity and a 15-V, 100-ns rectangular pulse was applied to generate ultrasound signals. The echo signals were amplified by a fixed gain of 60 dB. The amplified signals were sampled at a rate of 50 MHz and digitized with a resolution of 8 bits. The RF A-scans from all 128×128 transmit-receive element combinations were automatically acquired and stored for off-line digital processing.

In conventional phased array (CPA) ultrasound imaging, all array elements are fired simultaneously to form a beam with a fixed focus beyond the minimum $f_{\#}$ depth, whereas dynamic focusing is employed as all elements simultaneously receive the echo signal [39]. Having the full set of data consisting of all transmit-receive combinations allows emulation of any beamforming scheme through off-line processing. However, using only one element in transmit limits the total acoustic output power and hence degrades the SNR of the received echo signal from a single channel. In this experiment, signal averaging over 100 successive acquisitions was used to avoid low SNR in A-scans caused by the limited output power of a single transducer element. The averaged A-scans were stored with a 12-bit sample resolution. One should note that signal averaging over 100 acquisitions corresponds to a 20 dB SNR improvement whereas in phased array operation firing from 128 elements provides a 42 dB ($20log_{10}128$) SNR improvement.

B. Resolution Test Phantom

The resolution test phantom consisted of seven stainless steel wires, each having a diameter of 0.38 mm. The locations of wires were arranged in a diagonal fashion, so

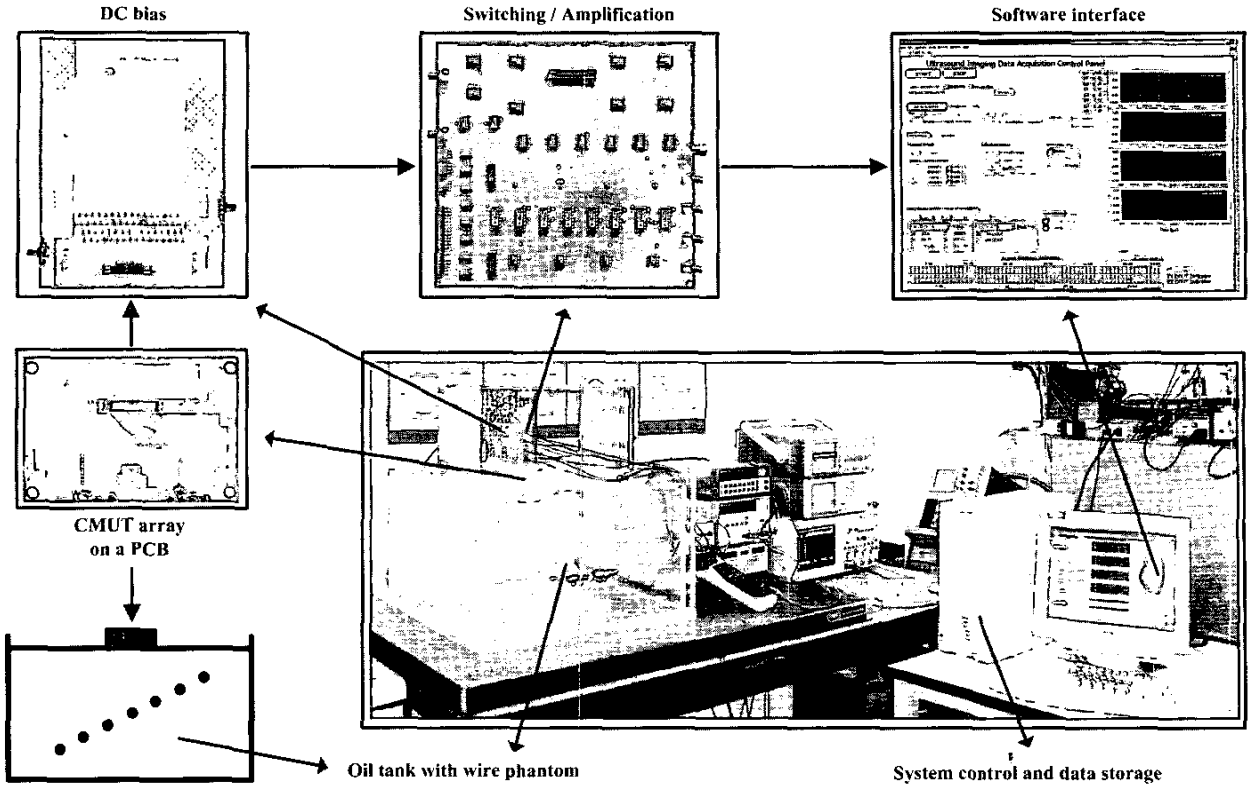

Fig. 4. Experimental data acquisition system.

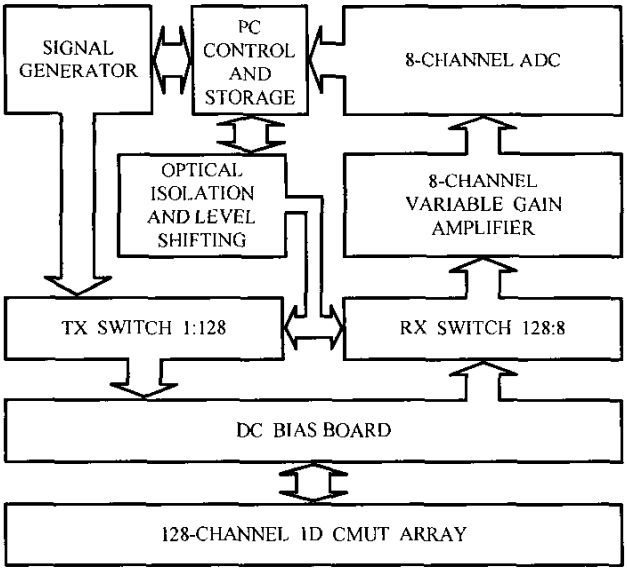

Fig. 5. Block diagram of the data acquisition system.

that the PSFs at different spatial locations could be tested. The wire phantom and the CMUT array were immersed in vegetable oil. The low electrical conductivity of vegetable oil provides a natural isolation between the unisolated bond wires on the CMUT array. Additionally, vegetable oil roughly mimics the attenuation of soft tissue. We measured the attenuation in oil as a function of frequency using the broadband, through-transmission technique and spectral analysis. For a wide variety of materials, attenuation increases with frequency according to a power-law relation: $\alpha = \alpha_0 f^b$, where α_0 and b are material dependent constants, and f is the frequency [40]. The result of our attenuation measurements in oil and the fitted least-squares line ($R^2 = 0.9768$) are shown in Fig. 6. According to these results, the attenuation function in oil can be written as

$$\alpha = 0.08 f^{1.85}, \tag{1}$$

where α is in units of decibels per centimeter and f is in units of megahertz. This result agrees with previously reported values [41]. For human tissues, α_0 varies between 0.4 dB/cm and 2 dB/cm, and often a linear frequency dependence is assumed [40]. Attenuation in oil is compared to fatty tissue ($\alpha = 0.40 f^{1.00}$) [42], and homogenized liver ($\alpha = 0.56 f^{1.12}$) [43] in Fig. 6.

C. Analysis of A-Scan Data

Fig. 7 shows a sample A-scan, the echo signal received by the 90th element when the 121st element was transmitting. The echo signals coming from seven different wires in the phantom are clearly identified in the figure. This A-scan shows echo signals corresponding to a depth of 210 mm. The amplitude of the echo signals reflected from the first and second wires were smaller than the echo from

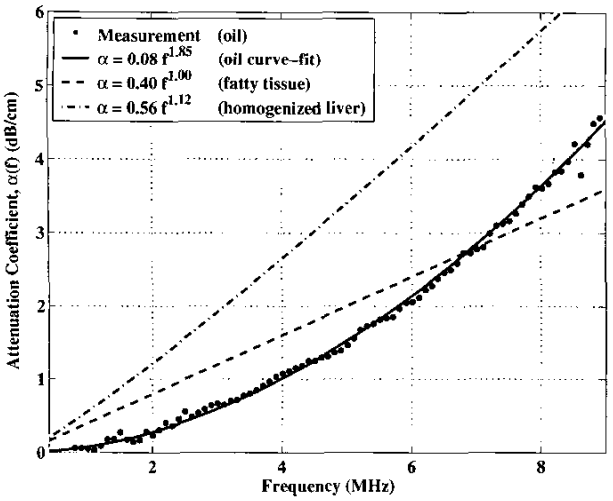

Fig. 6. Attenuation coefficient.

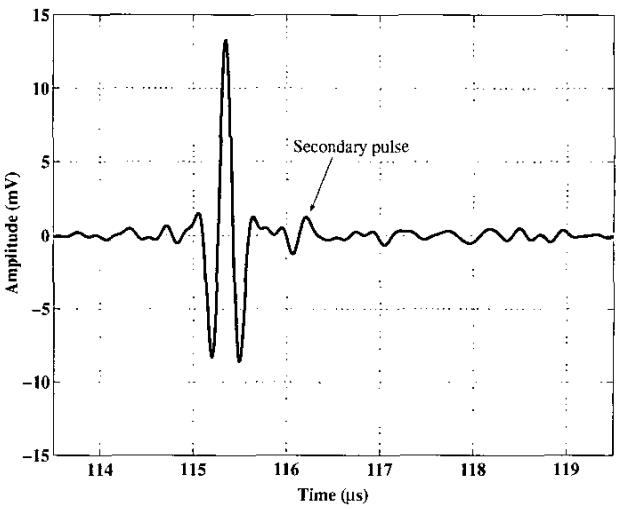

Fig. 8. Pulse-echo impulse response (echo signal from the third wire).

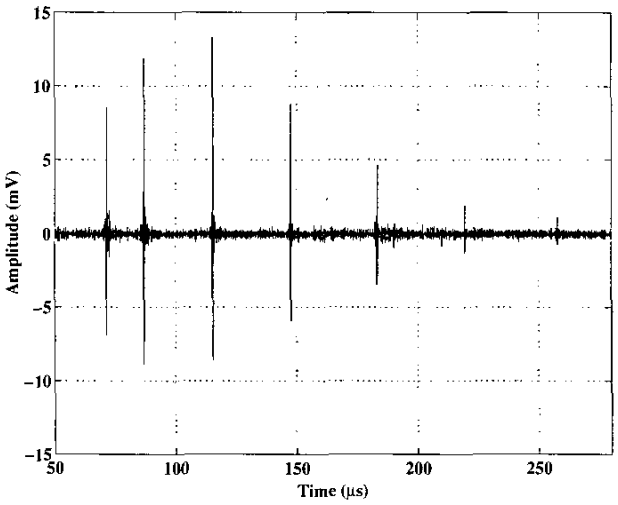

Fig. 7. A sample echo signal received by the 90th element when the 121st is transmitting.

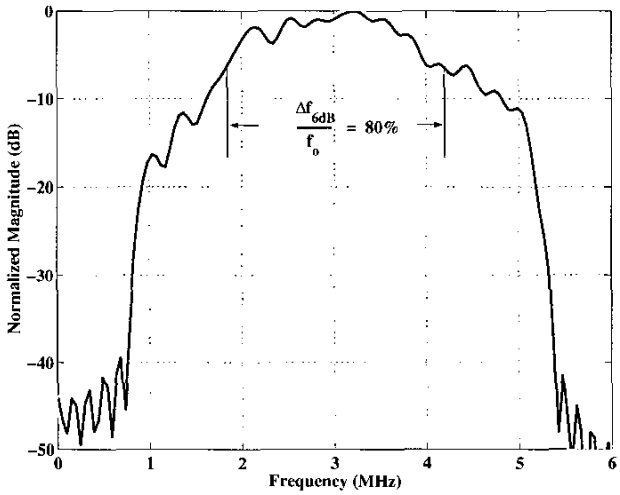

Fig. 9. Pulse-echo frequency response (Fourier transform of the echo signal from the third wire).

the third wire because the first two wires in the phantom were located at a larger angle off of the array normal. The lower echo amplitude for these echo signals was a result of the radiation pattern of a single transducer element. The theoretical 3-dB acceptance angle of a 200-μm wide ideal transducer element is 38 degrees when operating at 3 MHz. The lower amplitude of echo signals for wires beyond the third wire was due to the medium attenuation as discussed above. In this particular case, the difference between echo signal amplitudes from different depths was more than 20 dB.

We have chosen the echo signal coming from the third wire to represent the pulse-echo impulse response of the CMUT, as shown in Fig. 8. The third wire was chosen because of its proximity to the array normal and its midrange position resulting in the largest echo amplitude. The following secondary pulse was more than 20 dB lower than the main echo and is an indication of crosstalk between array elements [44], [45]. It has been reported [30] that Stoneley-type waves propagating at the fluid-silicon wafer interface and Lamb waves propagating in the silicon wafer are the major reasons for the crosstalk between array elements. The excitation mechanisms of these spurious modes have been investigated through radiation pattern and optical probe measurements. The details of the crosstalk characterization of 1-D CMUT arrays and several methods to reduce the crosstalk can be found in [30]. The effects of crosstalk on the reconstructed images are discussed in Section VI in this paper.

The pulse-echo frequency response was found by calculating the Fourier transform of the RF A-scan associated with the 3rd wire and is shown in Fig. 9. This response

was centered at 3 MHz and has a fractional bandwidth of 80%. Our previous measurements show that CMUTs have a fractional bandwidth of more than 100% [29]. In this case, the frequency-dependent attenuation in oil performs frequency shaping, effectively suppressing the high-frequency components of the signals when the propagation path is long, as in this experiment. The frequency response in Fig. 9 also includes the effect of a 1–5 MHz digital bandpass filter applied to eliminate out-of-band noise. The crosstalk between array elements also causes slight distortion and ripples at some frequencies in the pulse-echo frequency response. Currently, the acoustic coupling mechanisms and crosstalk reduction techniques are subjects of ongoing research.

We also performed an additional bandwidth measurement by obtaining a pulse-echo sample from a plane reflector (7-cm thick metal block) located at a distance of 10 mm. A 100-ns wide rectangular pulse was used to excite the 1-D CMUT array element. While keeping the DC bias board and the multiplexers, we bypassed the amplifier and the filter on the receive path to eliminate their effects on the output frequency spectrum. In order to reduce the total loss due to frequency-dependent attenuation in the medium, we placed the plane reflector close to the array. The resulting pulse-echo impulse response is shown in Fig. 10(a). The existence of the tail in this impulse response shows that the tail observed in wire echo signals was not due to reverberations in the wires and suggests that this tail was due to the crosstalk between array elements. The corresponding pulse-echo frequency response is shown in Fig. 10(b). This frequency response was centered at 4.59 MHz with a fractional bandwidth of 96%. Compensating for diffraction and attenuation losses resulted in a frequency response centered at 4.62 MHz with a 105% fractional bandwidth. This result indicates the wide bandwidth of CMUTs and confirms that the frequency spectrum of wire echo signals was significantly shaped by the frequency-dependent losses in the medium. One also should note that the compensated response still includes the frequency response of biasing and multiplexing circuits.

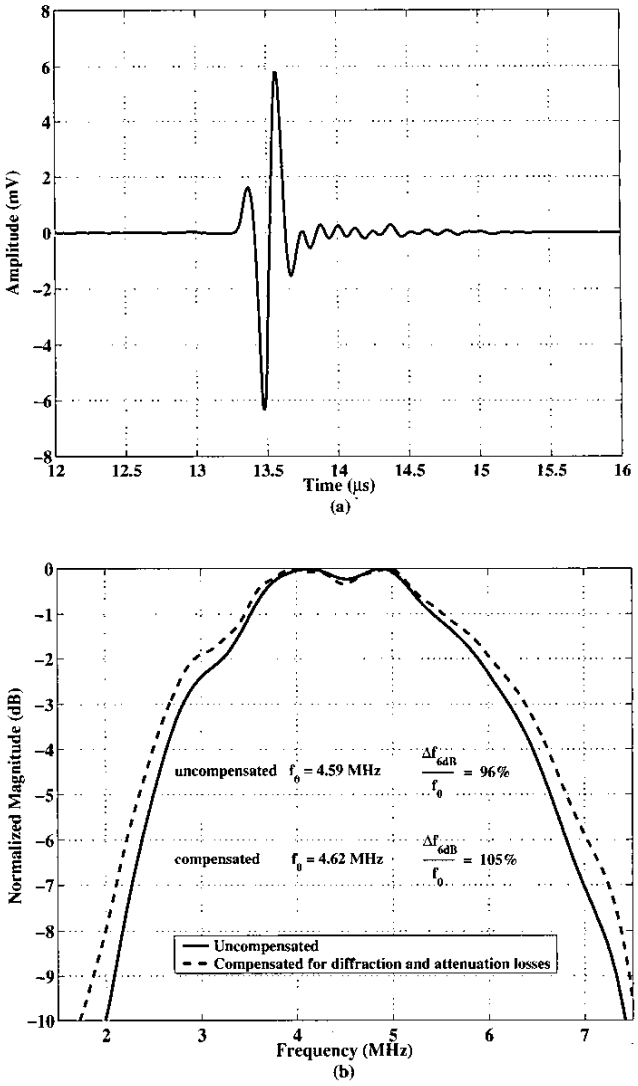

Fig. 10. (a) Pulse-echo impulse response measured from a plane reflector at a distance of 10 mm. (Amplifier and filter bypassed, no digital filtering applied, excitation: 100-ns wide unipolar pulse.) (b) Corresponding pulse-echo frequency response.

IV. Image Reconstruction

Following the acquisition of the complete data set for all 128×128 transmit-receive element combinations, the raw RF A-scan data were processed digitally to reconstruct the phased array B-scan sector image (Fig. 11). Prior to image reconstruction, a digital bandpass filter with a 1–5 MHz passband was applied to the raw data to eliminate out-of-band noise. The filtered signals were upsampled by a factor of two to prevent so-called "quantization lobes" caused by delay quantization errors [46]. At this point, optionally, the differences in amplitude of echo signals associated with different depths can be compensated by applying a variable gain amplification on A-scans. The image was reconstructed by using RF beamforming and synthetic phased

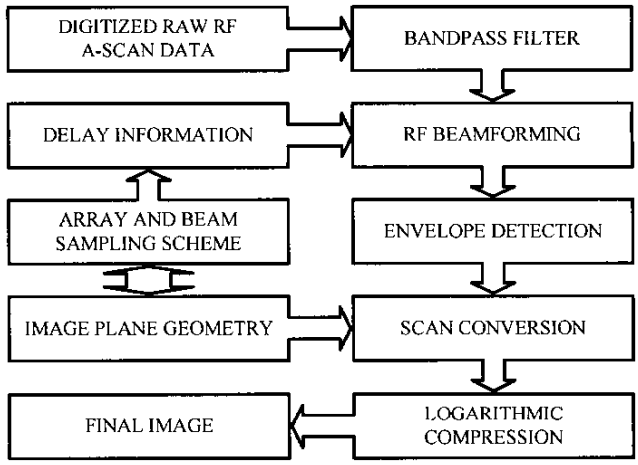

Fig. 11. Image reconstruction steps.

TABLE II
IMAGING PARAMETERS.

Depth of image, mm	210
Depth of dead zone, mm	37.5
Sector angle, *degrees*	90
Number of points along a beamline (P)	2500
Number of beamlines (Q)	300
f_s/f_0	33
Minimum f number ($f_\#$)	2
Pixel size in the sector image, mm^2	0.25 × 0.25

array approaches [47], [48]. In beamforming, the image sector first was sampled uniformly in the axial direction and uniformly in $\sin(\theta)$ in the lateral direction, where θ is the beam angle measured from the array normal. The image reconstruction parameters are given in Table II. The image formed using dynamic focusing both in transmit and receive beamforming using the complete data set with N^2 A-scans from an N-element array is considered as the highest quality image and, hence, this beamforming scheme is called the gold standard phased-array (GPA). Delay information for gold standard phased-array beamforming mentioned in Fig. 11 is a look-up table or a focus map with a complexity of $O(N \cdot P \cdot Q)$, where N is the number of transducer elements, P is the number of points along a beamline in the axial direction, and Q is the number of beamlines. These delays are calculated as follows:

$$\tau[n,p,q] = \frac{1}{c}(R[p] - \rho[n,p,q]), \tag{2}$$

where $\tau[n,p,q]$ is the delay applied to the nth channel for the pth pixel in the range direction of the qth beamline, and c is the speed of sound in the medium. This delay is basically the difference in time between flights from pixel to array-phase center ($R[p]/c$) and from pixel to the element under consideration ($\rho[n,p,q]/c$).

The beamforming can be expressed as:

$$U[p,q] = \sum_{i=1}^{N} a_i[p,q] \sum_{j=1}^{N} b_j[p,q] s_{ij}[k], \tag{3}$$

where

$$k = \text{round}\left\{ f_s \left(\frac{2R[p]}{c} - \tau[n_i,p,q] - \tau[n_j,p,q] - t_0 \right) \right\}. \tag{4}$$

In the expression above, $\tau[n_i,p,q]$ and $\tau[n_j,p,q]$ refer to delays applied during transmit and receive beamforming, respectively, $R[p]$ is the distance from the origin of the phase center to the focal point of interest ($[p,q]$), f_s is the sampling frequency of A-scans, and t_0 is the offset time. Here, $U[p,q]$ is the value of the image pixel in discrete *R-sin*(θ) space represented by sample indices (p,q), and $a_i[p,q]$ and $b_j[p,q]$ represent the weighting for the ith element during transmit and the jth element during receive operations, respectively. These weighting values are set to zero and nonzero values for $f_\#$ apodization. The rounding operation in (4) is performed to pick the closest sample to the calculated exact time point. Because the A-scans are sampled with a finite sampling rate, a rounding operation is necessary and causes the delay quantization error that can be minimized by upsampling the original signal. The ratio of the rms array/delay quantization errors to the main lobe amplitude is expressed as:

$$\frac{\text{rms quantization errors}}{\text{main lobe amplitude}} \approx \frac{\pi}{\mu\sqrt{6N}}, \tag{5}$$

where μ is the ratio of the sampling frequency to the center frequency of the ultrasound (f_s/f_o) [46]. According to this expression, 100 MHz sampling frequency results in quantization sidelobes 50 dB lower than the main lobe ($N = 128$, $f_o = 3$ MHz).

A minimum $f_\#$ of 2 was used by dynamically changing the aperture size with the depth to produce a smooth focus in the near field. This was achieved by using the look-up tables for a_i and b_j. The array was not apodized either in transmit or in receive, but used a rectangular aperture function ($a_i[q,p] = 1$ and $b_j[q,p] = 1$ beyond the minimum $f_\#$ range). After coherent image formation was completed, the envelope of the resulting image was detected. The image scans then were converted from polar to cartesian coordinates by using bilinear interpolation [49]. The logarithmic compressed final images were displayed in grey scale with display dynamic ranges of 40 dB and 60 dB.

The computational complexity of synthetic phased-array image reconstruction can be expressed as $O(N^2 \cdot P \cdot Q)$. This excludes the standard image processing operations such as scan conversion, envelope detection, and logarithmic compression, each with a computational complexity of $O(P \cdot Q)$. The total run time is machine dependent; in our case, it took approximately 30 minutes to reconstruct and display the image on a personal computer with a 1.8-GHz microprocessor (model Pentium 4, Intel Co., Santa Clara, CA).

V. ANALYSIS OF RESULTS

The final reconstructed GPA B-scan sector image with 210 mm image depth and 90 degrees sector angle is displayed at 40 and 60 dB dynamic display ranges in Fig. 12(a) and (b), respectively. The image of each wire target represents the PSF of the overall imaging system at that particular location on the imaging plane. The six reflectors identified in the B-scan images correspond to wires 2 to 7 in the phantom. Because the first wire's location is outside the 90-degree sector angle, it does not show up in the resulting images.

In this section, we primarily analyze the effects of wideband response of CMUTs on the resulting B-scan sector images. The PSF of the imaging system is the most important measurement to analyze these effects. An important property to recognize about the 2-D PSF of a wideband system is that it has a star-like shape, characterized by

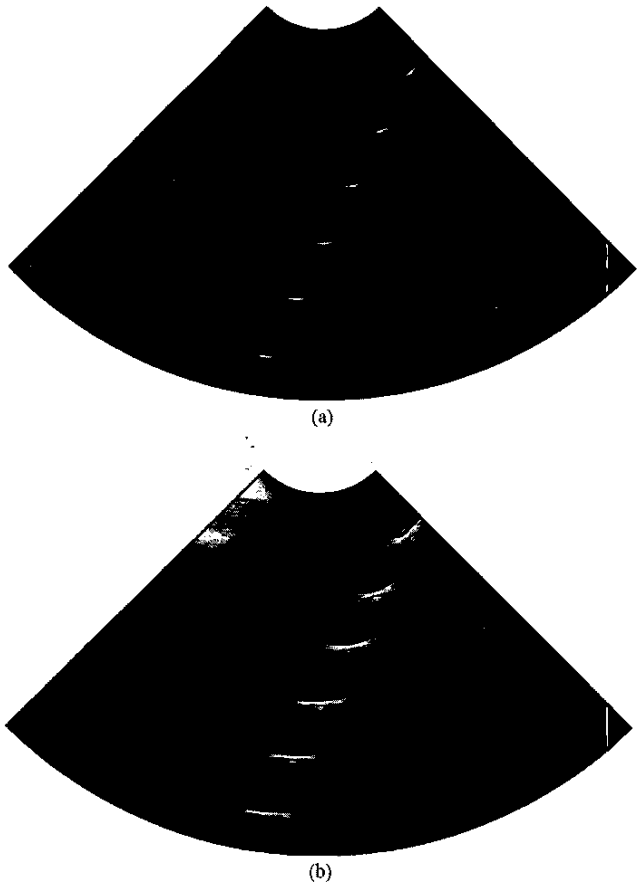

Fig. 12. Reconstructed GPA B-scan sector images with display dynamic ranges (a) 40 dB and (b) 60 dB.

diagonal "arms" that extend out from the mainlobe [50]. This star-like PSF is clearly identified in Fig. 12(b), especially from the second reflector shown in the image. The diagonal arms in the wideband 2-D PSF are a result of the fact that the lateral and axial responses interact with each other and are not separable as in the continuous wave (CW) case. As the signal bandwidth decreases, the diagonal "arms" become less visible. In the other extreme, as the signal bandwidth increases, a "bow-tie-like" shape aligned in the lateral direction is observed [50], [51].

The lateral cross section of the 2-D PSF is shown in Fig. 13. The lateral PSF was measured on the array normal at a distance of 135 mm from the array center. This measured lateral PSF was compared to the results of a numerical simulation for the pulsed transducer array. This simulation accounted for the angular response of an ideal single transducer element and frequency-dependent attenuation in the medium. There was no additive noise in the simulation data. The image was reconstructed from the simulated A-scans using the identical procedure for the experimental data as described in the previous section. A good agreement was observed between the experimental and simulation results. An important observation made on the lateral PSF is that it exhibited a smooth monotonic fall-off in amplitude. For conventional phased-array imaging, the two-way, quasi-CW unsteered lateral PSF is expressed as [47]:

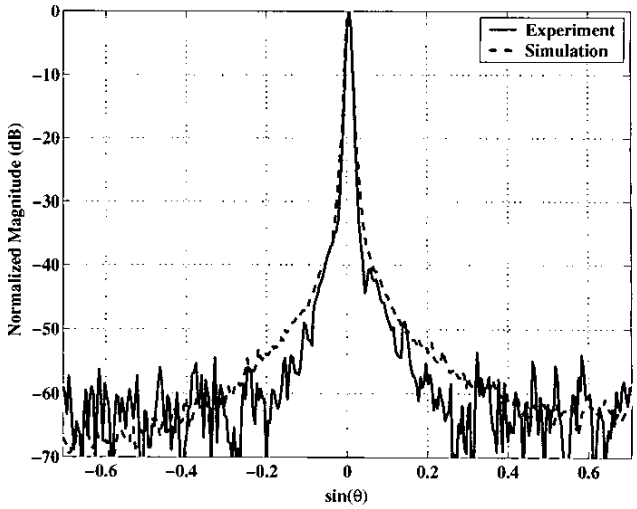

Fig. 13. Lateral point spread function on array normal at 135 mm.

$$h(\theta) \propto \frac{\sin^2(\frac{\pi N d}{\lambda}\sin\theta)}{\sin^2(\frac{\pi d}{\lambda}\sin\theta)}, \tag{6}$$

where $\lambda = c/f_o$ is the ultrasound wavelength in the medium. In the case of a wideband imaging system, sidelobe patterns from different frequency components in the signal band shift with frequency, whereas the main lobe stays at the center. This behavior results in a smooth fall-off in the sidelobes. This function can be regarded as the envelope of the sinc-like lateral PSF in the quasi-CW analysis. The lateral resolution of the imaging system represents the ability of the system to distinguish two neighboring point targets from each other and can be defined in different ways, such as using 6-dB rolloff points or the Rayleigh or Sparrow two-point definitions [52], [53]. We measured the full angular spread between the 6-dB points ($\Delta\theta_{6-dB}$) for the given PSF as 0.0144 radians, corresponding to an arc length of 1.94 mm at 135 mm depth. This result is in agreement with the 6-dB spread of the unsteered PSF in (6) evaluated at f_o. Note that the lateral resolution is a function of transmit and receive aperture functions. Thus, in conventional systems, aperture apodization is often used for sidelobe reduction at the expense of a wider mainlobe.

The axial resolution defines the ability of the system to distinguish targets spaced closely together in the axial direction. The axial resolution is determined by the effective duration of the ultrasonic pulse. The effective pulse duration is determined by the center frequency and the bandwidth of the transducer. The measured and simulated axial PSFs are shown in Fig. 14. The 6-dB resolution was measured as 0.3 mm at 135-mm depth. The wide bandwidth of CMUTs significantly increases the axial resolution. The mainlobe cross section of the PSF in the axial

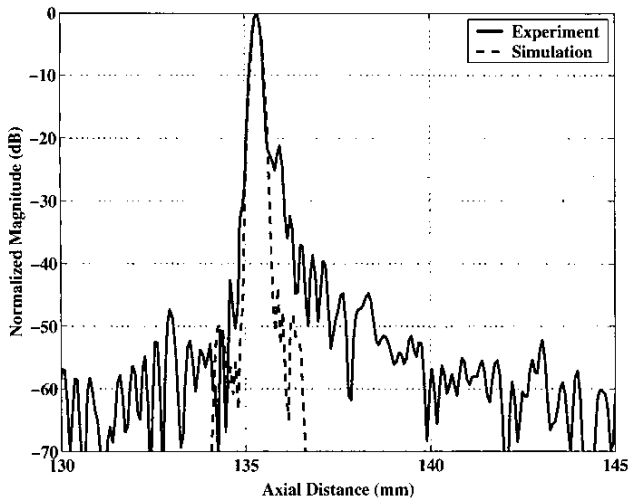

Fig. 14. Axial point spread function on array normal at 135 mm.

TABLE III
SUMMARY OF RESULTS.

Pulse-echo center frequency (f_0), MHz (including diffraction and attenuation losses)	3.0
Pulse-echo fractional bandwidth, % (including diffraction and attenuation losses)	80
Pulse-echo center frequency (f_0), MHz (compensated for diffraction and attenuation losses)	4.62
Pulse-echo fractional bandwidth, % (compensated for diffraction and attenuation losses)	105
Average A-scan SNR, dB	22
Average image SNR, dB	54
Lateral resolution ($\Delta\theta_{6-dB}$), radians (GPA, on array normal, r = 135 mm)	0.0144
Lateral resolution (Δs_{6-dB}), mm (GPA, on array normal, r = 135 mm)	1.94
Axial resolution (Δr_{6-dB}), mm (GPA, on array normal, r = 135 mm)	0.3

direction was in agreement with the simulation results. The measured axial PSF had a tail that was observed as a shadow behind the wire in the reconstructed images. The amplitude of this tail in the axial PSF was more than 20 dB lower than the mainlobe amplitude. This tail in the image should have been caused by the crosstalk between array elements as discussed in Section III. The 20-dB difference between the amplitude of the mainlobe and the tail was also in agreement with the 20-dB difference measured between the main wire echo and the following secondary pulse in the A-scan shown in Fig. 8.

Another important point to recognize in the reconstructed image is the grating lobe artifact observed at a 90 degree angle off of the first and second reflectors. Although the first reflector was not seen in the image, the grating lobe artifact associated with it was visible. The inter-element spacing of the array was 250 μm. This spacing satisfies the $\lambda/2$ spatial sampling criteria for frequency components up to 3 MHz. Because the CMUT array element had a broadband response, frequency components higher than 3 MHz caused the grating lobe artifact mentioned above. These grating lobes were more than 50 dB lower than the main lobe. The relative peak amplitude of the grating lobes is reduced by three factors. The first of these is the obliquity factor, the $cos^2(\theta)$ term [54]. The second factor is the unfocused, far-field beam pattern of a single element. The third factor reducing the grating lobes is the wideband nature of the system. For the first grating lobe, the amplitude is reduced by the ratio of the number of cycles in the pulse to the number of elements in the array [50].

The average SNR of the image was calculated by finding the average signal power in the 3-dB vicinity of six wire targets and dividing this average signal power to the average noise power sampled from different regions in the image. This average image SNR was found to be 54 dB, whereas the maximum SNR was measured for the third reflector as 57 dB. Assuming uncorrelated additive electronic noise during receive, the SNR improvement for gold standard phased array beamforming can be expressed in units of dB as:

$$\frac{\text{SNR}}{\text{SNR}_0} = 20log_{10}(N_t\sqrt{N_r}), \tag{7}$$

where SNR_0 is the SNR of a single A-scan, N_t is the number of elements in transmit aperture, and N_r is the number of elements in receive aperture. The relative SNR of synthetic GPA is:

$$\frac{\text{SNR}}{\text{SNR}_0} = 20log_{10}(\sqrt{N_tN_r}). \tag{8}$$

The SNR improvement by synthetic GPA beamforming was calculated as 42 dB for the 128-element array. The average SNR of A-scans (SNR_o) was measured as 22 dB, whereas the maximum SNR was measured for the third reflector as 25 dB. Accordingly, a 64-dB average image SNR was expected. However, any correlation between noise sources of different A-scans would result in a reduction of the SNR improvement by beamforming. In this case the difference between the expected average SNR of 64 dB and the measured average SNR of 54 dB was 10 dB, indicating that the noise sources were not fully uncorrelated.

The image also was constructed using CPA beamforming in which the fixed transmit focus was set at 110 mm. In this case, the transmit delay term ($\tau[n_i, p, q]$) in (4) was replaced with a constant delay calculated for the fixed transmit focus range for each beam. The CPA B-scan sector image is displayed in Fig. 15. The GPA and CPA images were identical around the fixed transmit focus for CPA beamforming. At other points in the CPA reconstructed image the degradation in spatial resolution was noticeable compared to the GPA reconstructed image. The results of the analysis carried out in this section are summarized in Table III.

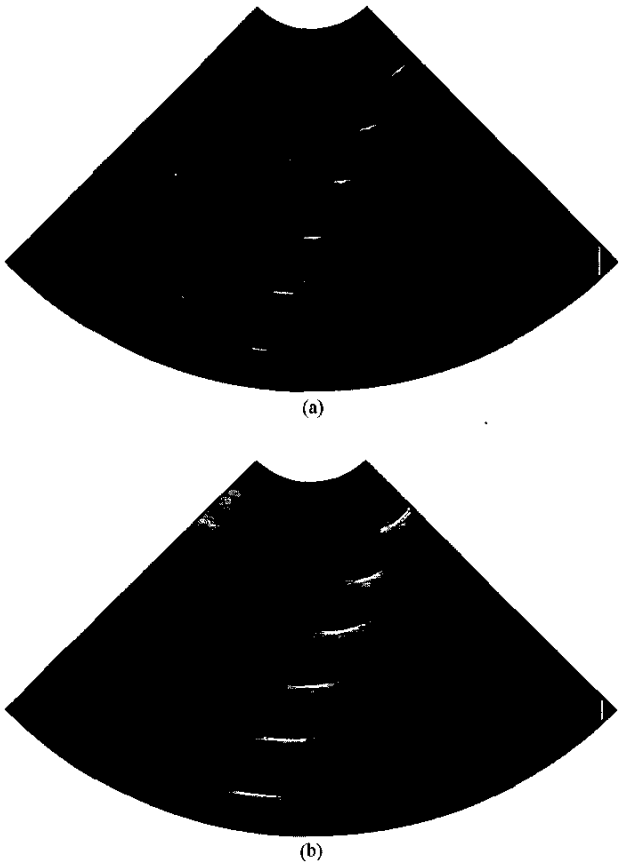

Fig. 15. Reconstructed CPA B-scan sector images with display dynamic ranges (a) 40 dB and (b) 60 dB.

VI. Discussion

The basic physical structure of the 1-D CMUT array used in this study was a solid silicon plate with fluid on one side and a solid PCB on the other side. These boundary conditions provide the environment for the excitation and propagation of various spurious modes such as Lamb waves and Stoneley-type waves. We recently performed studies on the characterization of the crosstalk mechanism in 1-D CMUT arrays and reported in [30].

To observe the effects of crosstalk on the image quality, we reconstructed the experimental B-scan images with a larger sector angle and a lower minimum $f_{\#}$ so that any artifacts in the far off-axis regions and in the near field of the array would be visible. The reconstructed experimental B-scan image scanned a sector from -70 to $+70$ degrees with a minimum $f_{\#}$ of 1, where the image depth extended from 7 mm to 210 mm. A simulated image of wire targets using ideal transducer elements also was produced to distinguish the artifacts due to imperfections in the array from those caused by the grating lobes, as well as to compare the resolution and contrast characteristics of measured versus theoretical. These experimental and simulated images are shown in Fig. 16(a) and (b), respectively.

Two crosstalk artifacts were observed in the experimental image: degradation in the axial resolution and bright patterns in the near field. We discussed the degradation of the axial resolution in Section V. The artifacts in the near field extended out from the array to a depth of 2 cm. These artifacts at the apex of the experimental sector image were 20 dB below the maximum brightness of the wire targets. Previously, it was shown that the direct propagation of the Stoneley-type waves and their reflection and mode conversion at the edge of the silicon substrate contribute to the crosstalk between elements [30]. The direct and reflected interface waves set any membrane along their path into motion. These signals constructed the bright patterns in the near field as if there were nearby reflectors. The distance between the edges of the artifacts observed in the near field in Fig. 16(a) agreed with the physical size of the array. This observation indicates that these artifacts were caused by the reflections of the spurious waves from the edges of the silicon substrate.

We also characterized the electrical crosstalk in the experimental system. As discussed in Section III-A, the transmit-receive electronics were built on PCBs, where the capacitance between long metal traces associated with different channels caused electrical coupling between neighboring channels. The nearest neighbor electrical crosstalk was measured as -32 dB relative to the excited element. The electrical crosstalk for the second and third nearest neighbors was measured as -38 dB and -45 dB, respectively.

Our current studies are focused on the investigation of crosstalk mechanisms and methods for their reduction through finite-element simulations and experimental characterization.

VII. Conclusions

We have presented the first pulse-echo phased-array B-scan sector images using a 128-element, 1-D linear CMUT array. Although the experimental setup used in this study was not necessarily optimal, the image quality achieved demonstrates the viability of CMUT technology for ultrasound imaging. The results presented in this paper confirm the wide bandwidth and high sensitivity of CMUTs from an imaging point of view.

We also performed preliminary analysis of the effects of crosstalk between array elements on the reconstructed image. We observed two artifacts due to crosstalk between array elements: bright patterns in the near field and a tail observed more than 20 dB lower than the mainlobe in the axial PSF. Understanding the crosstalk mechanism and devising methods to further reduce the crosstalk are subjects of our current research.

We continue to conduct extensive research in transducer design, beamforming algorithms, system design, and interface circuit design. Transducer design research includes analysis of crosstalk reduction by finite element methods, maximizing the acoustic output power for small AC voltage amplitudes, and further improvement of receive sensitivity. The system level research is focused on phased-

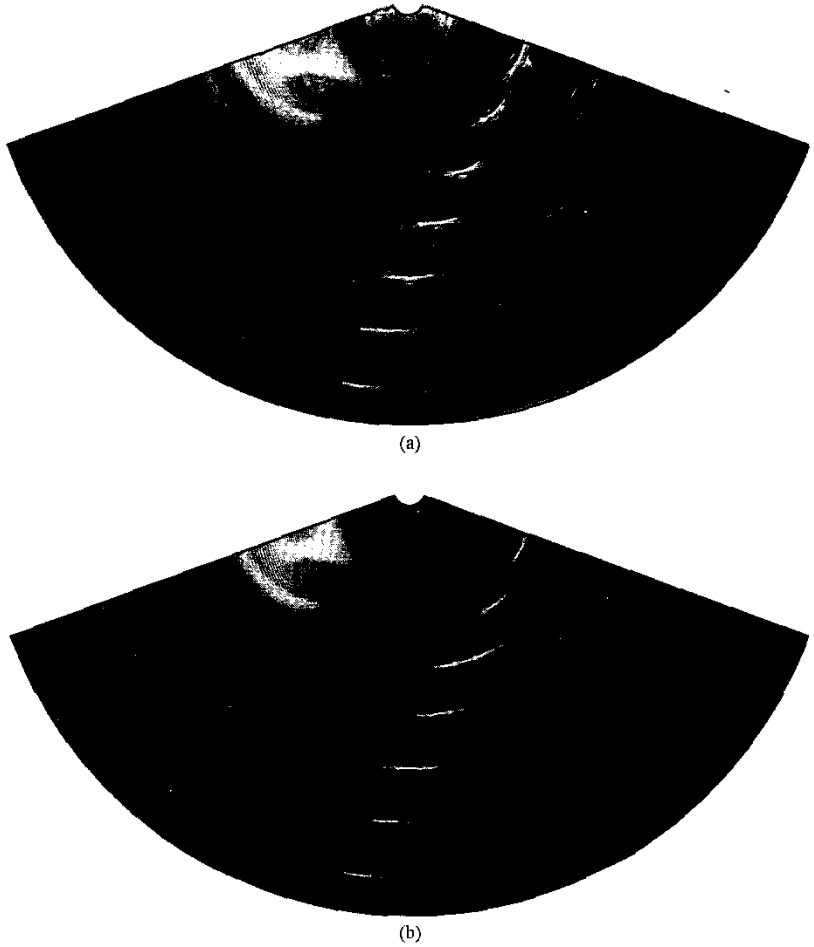

Fig. 16. Reconstructed GPA B-scan sector images (display dynamic range = 60 dB, sector angle = ±70 degrees, image depth = 7 mm–210 mm) (a) Experimental and (b) simulation with no additive noise.

subarray beamforming schemes to reduce hardware complexity for systems with fully populated large 1-D and 2-D arrays [55], [56]. Optimized front-end circuits and analog-to-digital converters are subjects of circuit level research [57].

We previously showed that silicon micromachining can be used to fabricate capacitive ultrasonic transducers which can compete with piezoelectric transducers in terms of efficiency and bandwidth. It also is well-known that CMUTs offer the promise of easier 1-D and 2-D array manufacturing and of integration with electronic circuitry. In this study, we have demonstrated the first full scale phased-array images using a large linear array based on CMUT technology. Based on this result, we firmly believe that CMUTs are a serious contender for the technology of choice in future ultrasonic imaging systems.

ACKNOWLEDGMENTS

The authors thank Aykutlu Dâna and Göksen Yaralıoğlu for useful discussions about instrumentation, Tim Brand for dicing the arrays, Pauline Prather for wire bonding, Larry Randall for his help with machining, and Murat Özsüt and Mehmet Yüksekkaya for their help in data analysis and PCB design.

REFERENCES

[1] F. V. Hunt, *Origins of Acoustics*. New Haven, CT: Yale Univ. Press, 1978.

[2] F. V. Hunt, *Electroacoustics: The Analysis of Transduction, and Its Historical Background*. New York: Acoustical Society of America, 1982.

[3] K. R. Erikson, F. J. Fry, and J. P. Jones, "Ultrasound in medicine—A review," *IEEE Trans. Sonics Ultrason.*, vol. SU-21, pp. 144–170, Jul. 1974.

[4] W. P. Mason, "Sonics and ultrasonics: Early history and applications," *IEEE Trans. Sonics Ultrason.*, vol. SU-23, pp. 224–232, Jul. 1976.

[5] W. D. O'Brien, Jr., "Assessing the risks for modern diagnostic ultrasound imaging," *Jpn. J. Appl. Phys.*, vol. 37, pp. 2781–2788, May 1998.

[6] W. A. Smith, "The role of piezocomposites in ultrasonic transducers," in *Proc. IEEE Ultrason. Symp.*, 1989, pp. 755–766.

[7] B. T. Khuri-Yakub, C.-H. Cheng, F. L. Degertekin, S. Ergun, S. Hansen, X. C. Jin, and Ö. Oralkan, "Silicon micromachined

ultrasonic transducers," *Jpn. J. Appl. Phys.*, vol. 39, pp. 2883–2887, May 2000.

[8] S. W. Smith, H. G. Pavy, Jr., and O. T. von Ramm, "High-speed ultrasound volumetric imaging system—Part I: Transducer design and beam steering," *IEEE Trans. Ultrason., Ferroelect., Freq. Contr.*, vol. UFFC-38, pp. 100–108, Mar. 1991.

[9] O. T. von Ramm, S. W. Smith, and H. G. Pavy, Jr., "High-speed ultrasound volumetric imaging system—Part II: Parallel processing and image display," *IEEE Trans. Ultrason., Ferroelect., Freq. Contr.*, vol. UFFC-38, pp. 109–115, Mar. 1991.

[10] D. H. Turnbull and F. S. Foster, "Beam steering with pulsed two-dimensional transducer arrays," *IEEE Trans. Ultrason., Ferroelect., Freq. Contr.*, vol. UFFC-38, pp. 320–333, Jul. 1991.

[11] C.-H. Cheng, E. M. Chow, X. C. Jin, S. Ergun, and B. T. Khuri-Yakub, "An efficient electrical addressing method using through-wafer vias for two-dimensional ultrasonic arrays," in *Proc. IEEE Ultrason. Symp.*, 2000, pp. 1179–1182.

[12] J. F. Kuhmann, M. Heschel, S. Bouwstra, F. Baleras, and C. Massit, "Through wafer interconnects and flip-chip bonding: A toolbox for advanced hybrid technologies for MEMS," in *Proc. EUROSENSORS XIII 13th Eur. Conf. Solid-State Transducers*, 1999, pp. 265–272.

[13] M. A. Averkiou, D. N. Roundhill, and J. E. Powers, "A new imaging technique based on the nonlinear properties of tissues," in *Proc. IEEE Ultrason. Symp.*, 1997, pp. 1561–1566.

[14] J. A. Hossack, P. Mauchamp, and L. Ratsimandresey, "A high bandwidth transducer optimized for harmonic imaging," in *Proc. IEEE Ultrason. Symp.*, 2000, pp. 1021–1024.

[15] H. Jagannathan, G. G. Yaralioglu, A. S. Ergun, F. L. Degertekin, and B. T. Khuri-Yakub, "Micro-fluidic channels with integrated ultrasonic transducers," in *Proc. IEEE Ultrason. Symp.*, 2001, pp. 859–862.

[16] F. L. Lizzi, M. Ostromogilsky, E. J. Feleppa, M. C. Rorke, and M. M. Yaremko, "Relationship of ultrasonic spectral parameters to features of tissue microstructure," *IEEE Trans. Ultrason., Ferroelect., Freq. Contr.*, vol. UFFC-33, pp. 319–329, May 1986.

[17] G. Cincotti, G. Loi, and M. Pappalardo, "Frequency decomposition and compounding of ultrasound medical images with wavelet packets," *IEEE Trans. Med. Imag.*, vol. 20, pp. 764–771, Aug. 2001.

[18] S. Hansen, N. Irani, F. L. Degertekin, I. Ladabaum, and B. T. Khuri-Yakub, "Defect imaging by micromachined ultrasonic air transducers," in *Proc. IEEE Ultrason. Symp.*, 1998, pp. 1003–1006.

[19] S. T. Hansen, A. S. Ergun, and B. T. Khuri-Yakub, "Improved modeling and design of microphones using radio frequency detection with capacitive micromachined ultrasonic transducers," in *Proc. IEEE Ultrason. Symp.*, 2001, pp. 961–964.

[20] N. Hall and F. L. Degertekin, "An integrated optical detection method for capacitive micromachined ultrasonic transducers," in *Proc. IEEE Ultrason. Symp.*, 2000, pp. 951–954.

[21] G. G. Yaralioglu, M. H. Badi, A. S. Ergun, C. H. Cheng, B. T. Khuri-Yakub, and F. L. Degertekin, "Lamb wave devices using capacitive micromachined ultrasonic transducers," *Appl. Phys. Lett.*, vol. 78, no. 1, pp. 111–113, Jan. 2001.

[22] M. I. Haller and B. T. Khuri-Yakub, "A surface micromachined electrostatic ultrasonic air transducer," in *Proc. IEEE Ultrason. Symp.*, 1994, pp. 1241–1244.

[23] D. W. Schindel and D. A. Hutchins, "The design and characterization of micromachined air-coupled capacitance transducers," *IEEE Trans. Ultrason., Ferroelect., Freq. Contr.*, vol. UFFC-42, pp. 52–58, May 1986.

[24] P. C. Eccardt, K. Niederer, T. Scheiter, and C. Hierhold, "Surface micromachined ultrasound transducers in CMOS technology," in *Proc. IEEE Ultrason. Symp.*, 1996, pp. 959–962.

[25] X. C. Jin, I. Ladabaum, and B. T. Khuri-Yakub, "The microfabrication of capacitive ultrasonic transducers," *IEEE/ASME J. Microelectromech. Syst.*, vol. 7, pp. 295–302, Sep. 1998.

[26] X. C. Jin, I. Ladabaum, F. L. Degertekin, S. Calmes, and B. T. Khuri-Yakub, "Fabrication and characterization of surface micromachined capacitive ultrasonic immersion transducers," *IEEE/ASME J. Microelectromech. Syst.*, vol. 8, pp. 100–114, Mar. 1999.

[27] W. P. Mason, *Electromechanical Transducers and Wave Filters*. New York: Van Nostrand, 1948.

[28] I. Ladabaum, X. C. Jin, H. T. Soh, A. Atalar, and B. T. Khuri-Yakub, "Surface micromachined capacitive ultrasonic transducers," *IEEE Trans. Ultrason., Ferroelect., Freq. Contr.*, vol. UFFC-45, pp. 678–689, May 1998.

[29] Ö. Oralkan, X. C. Jin, F. L. Degertekin, and B. T. Khuri-Yakub, "Simulation and experimental characterization of a 2-D capacitive micromachined ultrasonic transducer array element," *IEEE Trans. Ultrason., Ferroelect., Freq. Contr.*, vol. UFFC-46, pp. 1337–1340, Nov. 1999.

[30] X. C. Jin, Ö. Oralkan, F. L. Degertekin, and B. T. Khuri-Yakub, "Characterization of one-dimensional capacitive micromachined ultrasonic immersion transducer arrays," *IEEE Trans. Ultrason., Ferroelect., Freq. Contr.*, vol. UFFC-48, pp. 750–759, May 2001.

[31] A. Bozkurt, I. Ladabaum, A. Atalar, and B. T. Khuri-Yakub, "Theory and analysis of electrode size optimization for capacitive microfabricated ultrasonic transducers," *IEEE Trans. Ultrason., Ferroelect., Freq. Contr.*, vol. UFFC-46, pp. 1364–1374, Nov. 1999.

[32] G. Wojcik, J. Mould, P. Reynolds, A. Fitzgerald, P. Wagner, and I. Ladabaum, "Time-domain models of MUT array cross-talk in silicon substrates," in *Proc. IEEE Ultrason. Symp.*, 2000, pp. 909–914.

[33] B. Bayram, G. G. Yaralioglu, and B. T. Khuri-Yakub, "Influence of the electrode size and location on the performance of a CMUT," in *Proc. IEEE Ultrason. Symp.*, 2001, pp. 949–952.

[34] Y. Roh and B. T. Khuri-Yakub, "Finite element analysis of underwater capacitor micromachined ultrasonic transducers," *IEEE Trans. Ultrason., Ferroelect., Freq. Contr.*, vol. UFFC-49, pp. 293–298, Mar. 2002.

[35] X. C. Jin, F. L. Degertekin, S. Calmes, X. J. Zhang, I. Ladabaum, and B. T. Khuri-Yakub, "Micromachined capacitive transducer arrays for medical ultrasound imaging," in *Proc. IEEE Ultrason. Symp.*, 1998, pp. 1877–1880.

[36] Ö. Oralkan, X. C. Jin, K. Kaviani, A. S. Ergun, F. L. Degertekin, M. Karaman, and B. T. Khuri-Yakub, "Initial pulse-echo imaging results with one-dimensional capacitive micromachined ultrasonic transducer arrays," in *Proc. IEEE Ultrason. Symp.*, 2000, pp. 959–962.

[37] S. T. Hansen, A. Turo, F. L. Degertekin, and B. T. Khuri-Yakub, "Characterization of capacitive micromachined ultrasonic transducers in air using optical measurements," in *Proc. IEEE Ultrason. Symp.*, 2000, pp. 947–950.

[38] U. Demirci, Ö. Oralkan, J. A. Johnson, A. S. Ergun, M. Karaman, and B. T. Khuri-Yakub, "Capacitive micromachined ultrasonic transducer arrays for medical imaging: Experimental results," in *Proc. IEEE Ultrason. Symp.*, 2001, pp. 957–960.

[39] T. A. Shoup and J. Hart, "Ultrasonic imaging systems," in *Proc. IEEE Ultrason. Symp.*, 1988, pp. 863–871.

[40] P. N. T. Wells, *Biomedical Ultrasonics*. London: Academic, 1977.

[41] R. Chanamai and D. J. McClements, "Ultrasonic attenuation of edible oils," *J. Amer. Oil Chem. Soc.*, vol. 75, no. 10, pp. 1447–1448, Oct. 1998.

[42] T. D. Mast, "Empirical relationships between acoustic parameters in human soft tissues," *Acoust. Res. Lett. [Online]*, no. 1(2), pp. 37–42, Oct. 2000.

[43] H. Pauly and H. P. Schwan, "Mechanism of absorption of ultrasound in liver tissue," *J. Acoust. Soc. Amer.*, vol. 50, pp. 692–699, 1971.

[44] J. D. Larson, "Non-ideal radiators in phased array transducer," in *Proc. IEEE Ultrason. Symp.*, 1981, pp. 673–684.

[45] D. H. Turnbull and F. S. Foster, "Fabrication and characterization of transducer elements in two-dimensional arrays for medical ultrasound imaging," *IEEE Trans. Ultrason., Ferroelect., Freq. Contr.*, vol. UFFC-39, pp. 464–474, Jul. 1992.

[46] D. K. Peterson and G. S. Kino, "Real-time digital image reconstruction: A description of imaging hardware and an analysis of quantization errors," *IEEE Trans. Sonics Ultrason.*, vol. SU-31, pp. 337–351, Jul. 1984.

[47] M. Karaman, P.-C. Li, and M. O'Donnell, "Synthetic aperture imaging for small scale systems," *IEEE Trans. Ultrason., Ferroelect., Freq. Contr.*, vol. 42, pp. 429–442, May 1995.

[48] K. E. Thomenius, "Evolution of ultrasound beamformers," in *Proc. IEEE Ultrason. Symp.*, 1996, pp. 1615–1622.

[49] H. G. Larsen and S. C. Leavitt, "An image display algorithm for use in real-time sector scanners with digital scan converters," in *Proc. IEEE Ultrason. Symp.*, 1980, pp. 763–765.

[50] A. Macovski, "Ultrasonic imaging using arrays," *Proc. IEEE*, vol. 67, pp. 484–495, Apr. 1979.

[51] S. J. Norton, "Theory of acoustic imaging," Ph.D. dissertation, Stanford Electronics Lab., Stanford Univ, Stanford, CA, Tech. Rep. 4956-2, Dec. 1976.
[52] G. S. Kino, *Acoustic Waves: Devices, Imaging, and Analog Signal Processing*. Englewood Cliffs, NJ: Prentice-Hall, 1987.
[53] M. M. Goodsitt, P. L. Carson, S. Witt, D. L. Hykes, and J. M. Kofler, Jr., "Real-time B-mode ultrasound quality control test procedures: Report of AAPM ultrasound task group no. 1," *Med. Phys.*, vol. 25, no. 8, pp. 1385–1406, Aug. 1998.
[54] A. R. Selfridge, G. S. Kino, and B. T. Khuri-Yakub, "A theory for the radiation pattern of a narrow strip acoustic transducer," *Appl. Phys. Lett.*, vol. 37, no. 1, pp. 35–36, Jul. 1, 1980.
[55] M. Karaman and B. T. Khuri-Yakub, "Low-cost front-end processing for large array systems," in *Proc. 17th Int. Congr. Acoust. (ICA'01)*, 2001.
[56] J. A. Johnson, M. Karaman, and B. T. Khuri-Yakub, "Synthetic phased array image formation and restoration," in *Proc. IEEE Int. Conf. Acoust., Speech, Signal Processing*, 2002, pp. 2885–2887.
[57] K. Kaviani, Ö. Oralkan, B. T. Khuri-Yakub, and B. A. Wooley, "A multichannel, pipeline analog-to-digital converter for an integrated 3-D ultrasound imaging system," in *Proc. Eur. Solid-State Circuits Conf. (ESSCIRC'02)*, 2002, pp. 263–266.

Ömer Oralkan (S'93) was born in İzmit, Turkey, in 1973. He received the B.S. degree from Bilkent University, Ankara, Turkey, in 1995, and the M.S. degree from Clemson University, Clemson, SC, in 1997, both in electrical engineering. He is currently pursuing a Ph.D. degree in electrical engineering at Stanford University, Stanford, CA.

From 1995 to 1996, he was a hardware and network engineer at Bilkent University Computer Center, Ankara, Turkey. In the summer of 1997, he worked as a process engineer at the National Semiconductor Research Laboratories, Santa Clara, CA. His past and present research interests include analog and digital circuit design, micromachined sensors and actuators, and semiconductor device physics and fabrication. His current research focuses on front-end electronic circuit design for 2-D capacitive micromachined ultrasonic transducer arrays for hand-held 3-D ultrasonic imaging systems. He is a corecipient of the Best Paper award presented at the IEEE International Symposium on the Physical and Failure Analysis (IPFA). He is a member of IEEE.

A. Sanlı Ergun (S'96–A'98) was born in Ankara, Turkey, in 1969. He received his B.Sc., M.Sc., and Ph.D. degrees in 1991, 1994, and 1999, respectively, all in electrical and electronics engineering, from Bilkent University, Ankara, Turkey.

He was a research assistant in Bilkent University, Ankara, Turkey, between 1991 and 1999. He now is in the E. L. Ginzton Laboratory, Stanford University as an engineering research associate. His research interests are microwave electronics, ultrasonics, MEMS, and specifically CMUTs. He is a member of the IEEE and the Electron Devices Society.

Jeremy A. Johnson (S'92) received his B.S. in electrical engineering and a minor in mathematics with honors from Walla Walla College, College Place, WA, in 1997. He received his M.S. degree in electrical engineering from Stanford University, Stanford, CA, in 1999. He is currently pursuing a Ph.D. degree in electrical engineering from Stanford University.

He has several summers of industry experience. He worked as a software engineer at Interactive Northwest, Inc., Tualatin, OR, during the summer of 1995; worked as an ASIC design engineer at Intel, Hillsboro, OR, during the summers of 1996 and 1997; performed research in color science at Sony Research Laboratories, San Jose, CA, during the summer of 1998; performed research in computer vision at Hughes Research Laboratories, Malibu, CA, during the summer of 1999; and developed an endoscopic calibration routine for image-enhanced endoscopy at Cbyon, Inc., Palo Alto, CA, during the summer of 2000. His research areas include medical imaging, computer-aided diagnosis, and image-guided surgery.

Mustafa Karaman (S'88–S'89–M'89–M'93–M'97) received the B.Sc. degree from the Middle East Technical University, Ankara, Turkey, and the M.Sc. and Ph.D. degrees from Bilkent University, Ankara, Turkey, in 1986, 1988, and 1992, respectively, all in electrical and electronics engineering. From 1993 to 1994, he was a post-doctoral fellow in the Biomedical Ultrasonics Laboratory in the Bioengineering Department, University of Michigan, Ann Arbor.

From 1995 to 1996, he was on the faculty with the Electrical and Electronics Engineering Department of Kırıkkale University, Kırıkkale, Turkey, first as an assistant professor and later as an associate professor. In 1996, he joined Başkent University, Ankara, Turkey, as the Chairman of Electrical and Electronics Engineering and Acting Chairman of the Computer Engineering Department and served in founding these departments. He was a visiting scholar in the Biomedical Ultrasonics Laboratory at the University of Michigan, Ann Arbor, and in the E. L Ginzton Laboratory at Stanford University, Stanford, CA, in the summer terms of 1996–1997 and 1999, respectively. In 2000, he joined the E. L. Ginzton Laboratory at Stanford University, as a visiting faculty in electrical engineering, where he is currently working on signal processing and system design for ultrasonic imaging using capacitive micromachined ultrasonic transducer arrays.

In 1996, Dr. Karaman was awarded the H. Tuğaç Foundation Award of Turkish Scientific and Technical Research Council for his contributions to ultrasonic imaging. He is a member of the IEEE.

Utkan Demirci (S'01) received his B.S. degree from the University of Michigan, Ann Arbor, in 1999 with Summa Cum Laude, supported by the Full Presidential Scholarship from Turkish Ministry of Education, and the M.S. degree from Stanford University, Stanford, CA, in 2001, both in electrical engineering. He currently is pursuing a Ph.D. degree in electrical engineering from Stanford University.

His research interests are design of 1-D and 2-D CMUT arrays for medical ultrasound imaging, and micromachined flextensional transducers for high-resolution printing and ejection applications.

Kambiz Kaviani (S'97) received the B.S. degree in 1994 from Sharif University of Technology, Tehran, Iran, and the M.S. degree from Stanford University, Stanford, CA, in 1999, both in electrical engineering. He currently is pursuing a Ph.D. degree in electrical engineering at Stanford University.

During the summer of 1998, he was with RadioLAN Corporation in Sunnyvale, CA, where he was involved in the design of next generation 5-GHz wireless local area networks (WLAN). His current research interests are analog and mixed-signal VLSI data converters, RF circuits, and MEMS technologies. He was a member of the Iranian team in the 21st International Physics Olympiad, Groningen, the Netherlands.

Thomas H. Lee (S'87–M'87) received the S.B., S.M., and Sc.D. degrees in electrical engineering from the Massachusetts Institute of Technology, Cambridge, in 1983, 1985, and 1990, respectively.

In 1990, he joined Analog Devices, Wilmington, MA, where he was primarily engaged in the design of high-speed clock recovery devices. In 1992, he joined Rambus Inc., Mountain View, CA, where he developed high-speed analog circuitry for 500-MB/s CMOS DRAMs. He has also contributed to the development of phase-locked loops (PLLs) in the StrongARM, Alpha, and K6/K7 microprocessors. Since 1994, he has been a professor of electrical engineering at Stanford University, Stanford, CA, where his research focus has been on gigahertz-speed wireline and wireless ICs built in conventional silicon technologies, particularly CMOS.

Dr. Lee cofounded Matrix Semiconductor, authored the textbook, *The Design of CMOS Radio-Frequency Integrated Circuits* (Cambridge, U.K.: Cambridge Univ. Press, 1998) and co-authored three books on RF circuit design. He holds 14 U.S. patents.

He is a Distinguished Lecturer of the IEEE Solid-State Circuits Society and the IEEE Microwave Theory and Techniques Society (IEEE MTT-S). He is a two-time recipient of the Best Paper Award presented at the International Solid-State Circuits Conference, a recipient of the Best Paper prize presented at the CICC and co-recipient of a Best Student Paper presented at the International Solid-State Circuits Conference (ISSCC). He holds a Packard Foundation Fellowship.

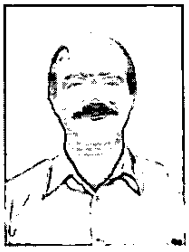

Butrus T. Khuri-Yakub (S'70–S'73–M'76–SM'87–F'95) was born in Beirut, Lebanon. He received the B.S. degree in 1970 from the American University of Beirut, the M.S. degree in 1972 from Dartmouth College, Hanover, NH, and the Ph.D. degree in 1975 from Stanford University, Stanford, CA, all in electrical engineering.

He joined the research staff at the E. L. Ginzton Laboratory of Stanford University in 1976 as a research associate. He was promoted to a senior research associate in 1978 and to a professor of electrical engineering (research) in 1982. He has served on many university committees in the School of Engineering and the Department of Electrical Engineering at Stanford University. Presently, he is the Deputy Director of the E. L. Ginzton Laboratory.

Dr. Khuri-Yakub has been teaching at both the graduate and undergraduate levels for over 15 years. His current research interests include in situ acoustic sensors (temperature, film thickness, resist cure, etc.) for monitoring and control of integrated circuits manufacturing processes, micromachining silicon to make acoustic materials and devices such as airborne and water immersion ultrasonic transducers and arrays, and fluid ejectors, and in the field of ultrasonic nondestructive evaluation and acoustic imaging and microscopy.

Dr. Khuri-Yakub is a fellow of the IEEE, a senior member of the Acoustical Society of America, and a member of Tau Beta Pi. He is associate editor of *Research in Nondestructive Evaluation,* a Journal of the American Society for Nondestructive Testing. He has authored over 300 publications and has been principal inventor or coinventor of 52 issued patents. He received the Stanford University School of Engineering Distinguished Advisor Award, June 1987, and the Medal of the City of Bordeaux for contributions to NDE, 1983.